Journal of Thermal Engineering
https://jten.yildiz.edu.tr/
https://doi.org/10.47481/jten.0060

RESEARCH ARTICLE

Study of MHD Casson blood flow in an inclined multi-stenosed artery with chemical reaction effects

Parth Patel[1], Rajiv Singh[2,*], Harshad Patel[3]

[1]Research Scholar, Gujarat Technological University, Ahmedabad, 382424, India
[2]Government Engineering College, Dahod, 389151, India
[3]U. V. Patel College of Engineering, Ganpat University, Mehsana, Gujarat, 384012, India

Abstract

This paper investigates the effects of chemical reactions on MHD Casson blood flow in an inclined artery with multiple stenoses. The flow is confined by external magnetic fields and an oscillating pressure gradient. The dimensionless form of the governing equations is remodeled into a system of time-fractional partial differential equations. For greater insight into the problems and to understand flow behavior, the Caputo time fractional derivative is used, which is also useful for representing memory effects in tissues and anomalous diffusion. The governing time-fractional differential equations are solved analytically using the Laplace transform to treat the temporal fractional derivative and finite Hankel transforms to handle the artery's radial geometry. To better understand the effects of different physical parameters on the profiles of blood velocity, magnetic particle velocity, heat transfer, and mass transfer, numerical results are obtained and presented in the graphs. Graphs indicate that the external magnetic fields tend to delay the blood flow motions, whereas, the Casson fluid parameter has an increasing impact on it. It is also observed that the heat source parameter enhances the heat transfer process. We have noted that increasing the systolic pressure gradient from 0.5 to 1.5 raises blood flow velocity by up to 78%, and increases magnetic particle velocity by up to 85%, and that increasing the Hartmann number controls the velocity by up to 70%. In short, the novelty of the article lies in modelling MHD flow in the presence of a multi-stenosed inclined artery, with the exact solution influenced by metabolic heat generation and chemical reaction. By acknowledging the non-Newtonian nature of blood and the influence of these factors, these studies pave the way for improved diagnostic tools and treatment strategies for cardiovascular diseases. Future research can build upon these findings by exploring potential therapeutic applications of magnetic fields or thermal interventions.

Keywords: Multi-stenosed artery, chemical reaction, magnetic field, Casson fluid, fractional derivative

Cite this article as: Patel, P., Singh, R., & Patel, H. (2026). Study of MHD Casson blood flow in an inclined multi-stenosed artery with chemical reaction effects. Journal of Thermal Engineering, 12(5), 1711–1722. https://doi.org/10.47481/jten.0060

1. Introduction

Unlike Newtonian fluids, non-Newtonian fluids do not exhibit a constant linear relationship between shear stress and the rate of deformation. This deviation arises because non-Newtonian fluids exhibit complex behavior, such as shear-thinning or shear-thickening, in which the viscosity changes with the shear rate. Blood is a complex suspension of cells, plasma, and other components, does not exhibit Newtonian fluid properties and therefore cannot be accurately modelled as such. In the mid-20th century, blood was assumed to behave as a Newtonian fluid to simplify mathematical modelling. However, as the need for more realistic models grew, it became evident that this assumption was insufficient to capture the true behavior of blood, particularly in the complex geometries of stenosed arteries. To gain a better understanding and to avoid limitations, many scholars have adopted non-Newtonian models, especially the Casson fluid model, which describes shear-thinning behavior of blood flow in pathological conditions such as a stenosed artery.

The Casson fluid model effectively captures the blood flow characteristics, especially when the flow involves large deformations or occurs through constricted or irregular geometries,

*Corresponding Author
E-mail Adress: singhrajiv.bhu@gmail.com

Submitted: 10 May 2025; **Accepted:** 19 August 2025

This paper was recommended for publication in revised form by Editor-in-Chief Ahmet Selim Dalkılıç

Published by Yıldız Technical University, İstanbul, Türkiye

for example in stenosed arteries. Many researchers have used this model to understand the nature of blood flow in stenoses of different shapes and under different conditions. Dash et al. [1] declared the effect of shear rate on the viscosity of the fluid as it attains zero when we increase the value of shear rate infinitely, which represents the property of shear thinning. Ali et al. [2] studied the unsteady MHD convective flow of Casson hybrid on the oscillating plate, which helps to understand how useful the magnetic fields are, on the flow of non-Newtonian fluids. Raghunatha et al. [3] worked by considering porous medium and flowing Casson fluid in presence of internal heat source, he reveals that how heat and magnetic field plays a vital role on the flow dynamics. Mukhopadhyay et al. [4] concluded that to control the separation of flow we can increase the Casson fluid parameter, which is a key factor in fluid dynamics. Other researchers, such as those by Afikuzzaman et al. [5] and Kataria and Patel [6], have considered past oscillating vertical plates and they focused on unsteady natural convective MHD Casson fluid flow, they contribute by concluding very important insights in behavior of fluid under the different conditions. Nandhini et al [7] modelled Casson fluid over a convective stretching sheet. Gupta et al [8] worked on the influences of buoyancy forces of MHD flow and induced by 3D exponential sheet. Dang et al [9] developed a model to explore the impacts of stream flow on the motion of an MHD non-Newtonian fluid through a permeable extending surface. Makkar et al [10] considered steady boundary layer with Casson nano fluid on the stretching sheet and studied numerically. Recently, the Casson fluid model has attracted the attention of lot of research scholars due to its high accuracy to represent the nature of blood, Casson fluid model is capable to reflect more realistic fluid characteristic in various physiological and pathological conditions, such as in arteries with stenosis [11-13]. This part contributes to understanding Casson fluid behavior in stenosed arteries of different shapes. The main cause of this study is that many research scholars worked on single stenoses or omitted the simultaneous effects of chemical reaction, metabolic heat, and fractional-order modelling, which are crucial for modelling physiological conditions.

In this line of research on blood flow through stenosed arteries, many researchers have investigated how arterial narrowing affects flow patterns, velocity distribution, and shear stress. One researcher Roy et al. [14] worked to understand more the changes in flow profiles by considering different shape stenoses and he noted that in his work. Ismail et al. [15] also contribute by considering the flood flow through tapered overlapping; by his work he concludes that how the varying cross-sectional areas influenced flow dynamics. Bakheet et al. [16] reach to the conclusion that how the inclination angle of stenotic arteries is very effective on the blood flow behavior, In the study of Ku [17] we can get fundamental insights into the behavior of blood flow in arteries, stressing the reduction in flow rate after passing through the stenosis region, as supported by Akhtar et al. [18]. Chakravarty et al. [19] concluded huge response of blood flow in the presence of heat and mass transfer with the help of graphical approach; by his work he declared the combined influence of thermal and mass diffusion. By considering the tapered artery. Mwapinga [20] highlighting the physiological relevance of stenosis in medical diagnostics. Deka et al [21] studied MHD fluid flow on an inclined surface with diffusion-thermo they reported the impacts of various parameters on heat and mass transfer in the MHD flow. In this part, references are thematically organized according to different stenosis geometries and to heat and mass transfer.

In recent years, researchers have frequently used fractional derivatives to model complex systems, especially in biology. This derivative facilitates a better understanding of fluids compared with the traditional integer derivative. This technique provides greater accuracy and flexibility in modelling real-world phenomena, particularly for blood flow behavior in arteries, where interactions are not simply local or instantaneous. Concept of Caputo-Fabrizio fractional-order model is used in the work of Jamil [22] to the nonlinear governing equations; by applying this concept he gets more accurate solution for complex fluid dynamics. Additionally, Rahman et al. [23] used the fractional Caputo-Fabrizio operator to demonstrate its utility in modelling biological processes by solving nonlinear fractional differential equations in biological population models. To show that the fractional order model is more capable of representing the complex behavior of the system which includes some complex conditions Ahmed et al. [24]. Even in the understanding of image processing Jain et al. [25] used fractional derivatives.

Within the field of fluid dynamics chemical reactions have attracted considerable attention from researchers in recent years. This study aims to understand the influence of chemical reactions on the unsteady hydromagnetic boundary-layer flow of a Casson fluid. Kataria et al [26] Concluded that an increase in the chemical reaction parameter led to a decrease in concentration in his work. Similarly, to highlight the significant influences of the chemical reaction in the presence of heat and mass transfer, Patel [27] considered a porous medium and published an article examining it. From the study above, chemical reactions in this line of study, particularly under pathological conditions, can alter the concentration of various blood components. Recently, it has been noted that not only single-stenosed but multi-stenosed arteries are common in humans. To deal with this problem Shahzad [28] studied by considering multi stenosed which are in elliptic shapes artery blood flow using the Carreau model to account for the non-Newtonian nature of blood. In addition, Kabir [29] added his work to note the influences in presence of multiple stenoses on blood flow behavior; by his work he concludes huge insights into cardiovascular risk assessment and the importance of considering multi-stenotic conditions in clinical evaluations. Yadav et al [30] prepared numerical 3D model of MHD flow with chemical reaction effects on permeable sheet and noted the impacts of different parameters. In this section, references are provided for models that were solved analytically by incorporating MHD Casson fluid, fractional time derivatives, chemical reaction, multi-stenotic inclined artery geometry, and metabolic heat effects; the Laplace and finite Hankel transforms were used to obtain exact solutions.

In this paper, through a thorough combination of various physical effects, this research uniquely combines the study of magnetic field, metabolic heat source, systolic and diastolic pressure gradients, Peclet number, Reynolds number, inclination-angle parameter, and heat absorption effects on blood flow in multiple-stenosed arteries, providing a more complete understanding of the complex flow dynamics. While previous studies have examined these phenomena separately, their combined impact on flow in multiple stenosed arteries has not been thoroughly investigated. This research paper will help in understanding blood flow dynamics in the presence of a multi-stenosed artery. We have modelled MHD fluid of fractional order in an artery with multiple stenoses, subject to chemical reactions and heat generation. Using analytical techniques, we found an exact solution of the system of PDEs and noted the effects of different parameters. This study introduces a novel analytical framework to explore the interplay among magnetic fields, metabolic heat generation and absorption, and their effects on blood flow and plaque dynamics in stenosed arteries, with therapeutic implications for cardiovascular treatments, hyperthermia therapies, and stenosis treatment. This study helps elucidate how parameters can improve medical treatments, particularly for conditions such as arterial blockage and targeted drug delivery systems.

The future scope of this study to extend with consideration mass transfer and various physical parameter effects like, chemical reactions, thermos-diffusion, diffusion thermos, etc.

2. Mathematical formulation

Recent research has focused on unsteady Casson blood flow, whose physical dimension is shown in Figure 1. In Figure 1, the z-axis is considered axial direction, while the r-axis indicates radial direction. Blood is treated as a non-Newtonian Casson fluid subjected to an oscillating pressure gradient (Jamil et al. [31]). The uniform external magnetic fields B_0 is applied which is shown in Figure 1. At t=0, the velocity of blood and magnetic particle are treated as stationary. Blood flow is modelled using the Navier–Stokes equations, whereas heat and mass transfer profiles are modelled using the energy and concentration equations. The effects of magnetic fields are described by Maxwell's relation, whereas magnetic particle velocity is governed by Newton's second law.

The constitutive equation for the Casson fluid can be written as given by Hayat et al. [32]

$$\tau_{ij} = \begin{cases} 2\left(\mu B + \dfrac{Py}{\sqrt{2\pi}}\right)e_{ij} & \pi > \pi_c \\ 2\left(\mu B + \dfrac{Py}{\sqrt{2\pi_c}}\right)e_{ij} & \pi < \pi_c \end{cases} \tag{1}$$

Where $\pi = e_{ij}e_{ij}$ and e_{ij} is the $(i, j)^{th}$ component of the deformation rate, π is the product of the component of deformation rate with itself, π_c is a critical value of this product based on the non- Newtonian model, μB is plastic dynamic viscosity of the non-Newtonian fluid and P_y is yield stress of fluid.

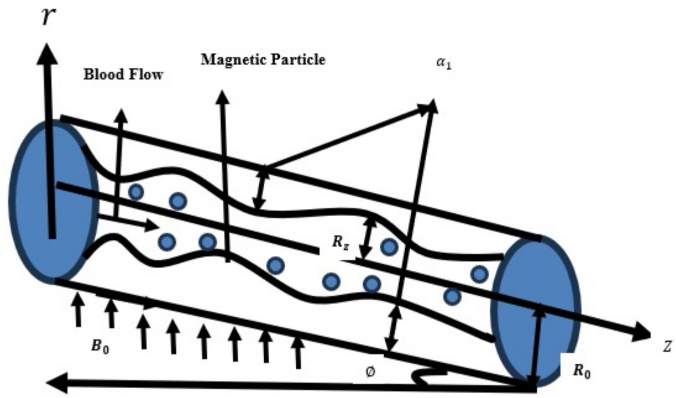

Figure 1. Schematic diagram of the flow geometry of the model

The pressure gradient can be expressed as,

$$-\frac{\partial P}{\partial z} = b_0 + b_1 \cos(\omega t),\ \ A_0 > 0 \tag{2}$$

Where constant A_0 is the systolic pressure gradient and A_1 is the diastolic pressure gradient components. The angular frequency as $\omega = 2\pi f_p$ where f_p is the frequency of the pulse.

Geometrically, the expression of multi-stenosis in the artery can be written mathematically,

$$R_z = 1 - \alpha_1\begin{pmatrix} 1.48x - 0.739x^2 + 0.148x^3 - 0.013955x^4 + 0.0006145x^5 \\ -0.000010243x^6 \end{pmatrix} \tag{3}$$

Where, R_z and R_0 represent the constricted region and normal artery radius. x is the stenosed length and α_1 stenosis degree.

The governing momentum equations of blood flows in cylindrical form is expressed as follows (Shah et al. [33]).

$$\frac{\partial u}{\partial t} = -\frac{1}{p}\frac{\partial p}{\partial z} + v\left(1 + \frac{1}{\gamma}\right)\left(\frac{\partial^2 u}{\partial r^2} + \frac{1}{r}\frac{\partial u}{\partial r}\right) + \frac{KN}{\rho}(v - u) - \frac{\sigma\beta_0^2 \sin\theta}{\rho}u + g\sin\ \emptyset \tag{4}$$

Due to Newton's second law governing the movement of magnetic particles:

$$m\frac{\partial v}{\partial t} = K(u - v) \tag{5}$$

Where m-average mass of magnetic particles.

The governing energy equation in the cylindrical form as,

$$\frac{\partial T}{\partial t} = \frac{K_1}{\rho C_p}\left(\frac{\partial^2 T}{\partial r^2} + \frac{1}{r}\frac{\partial T}{\partial r}\right) + \frac{Q_m + \theta_m}{\rho C_p} \tag{6}$$

The blood is considered as an optical thin fluid with low relative density and heat absorption coefficient So the heat flux can be approximated as

$$-\frac{\partial q}{\partial r} = 4\alpha_1^2(T - T_\infty) \quad (7)$$

Where, $\alpha_1^2 = \int_0^\infty \eta\chi\frac{\partial B}{\partial T}$, with η being the radiation absorption coefficient, χ is the frequency and B is the Planck's constant.

The concentration equation in the cylindrical form as,

$$\frac{\partial C}{\partial t} = D_m\left(\frac{\partial^2 C}{\partial r^2} + \frac{1}{r}\frac{\partial C}{\partial r}\right) + \frac{D_m K_T}{T_\infty}\left(\frac{\partial^2 T}{\partial r^2} + \frac{1}{r}\frac{\partial T}{\partial r}\right) - Kr(C - C_\infty) \quad (8)$$

The initial and boundary condition in cylindrical form with cylindrical domain and multi-stenosed artery of Radius R_0 and R_z are as,

$$u(r,0) = v(r,0) = T(r,0) = C(r,0) = 0 \text{ at } r \in [0, R_z]$$

$$u(r,t) = v(r,t) = T(r,t) = C(r,0) = 0 \text{ at } r = R_z \quad (9)$$

The non-dimensional parameters can be expressed as,

$$r^* = \frac{r}{R_0},\ t^* = \frac{t}{\lambda},\ u^* = \frac{u}{u_0},\ A_0^* = \frac{\lambda A_0}{\rho u_0}, A_1^* = \frac{\lambda A_1}{\rho u_0},$$

$$\omega^* = \lambda\omega,\ g^* = \frac{g}{\frac{u_0^2}{R_0}}$$

The governing dimensionless form of governing equation subject to equations (9) after dropping * notation, we can be written in form as,

$$\frac{\partial u}{\partial t} = b_0 + b_1\cos(\omega t) + \frac{1}{R_e}\left(1 + \frac{1}{\gamma}\right)\left[\frac{\partial^2 u}{\partial r^2} + \frac{1}{r}\frac{\partial u}{\partial r}\right] + R(v - u)$$

$$-Ha^2 u + \frac{\sin \emptyset}{F} \quad (10)$$

$$G\frac{\partial v}{\partial t} = u - v \quad (11)$$

$$P_e\frac{\partial \theta}{\partial t} = \left(\frac{\partial^2\theta}{\partial r^2} + \frac{1}{r}\frac{\partial\theta}{\partial r}\right) + P_e(Q_m + \theta_m) \quad (12)$$

$$S_c R_e\frac{\partial C}{\partial t} = \left(\frac{\partial^2 C}{\partial r^2} + \frac{1}{r}\frac{\partial C}{\partial r}\right) + S_r S_c\left(\frac{\partial^2\theta}{\partial r^2} + \frac{1}{r}\frac{\partial\theta}{\partial r}\right) - S_c R_e^2 KrC \quad (13)$$

With boundary conditions

$$u\left(\frac{r}{R_z},0\right) = 0,\ v\left(\frac{r}{R_z},0\right) = 0,\ \theta\left(\frac{r}{R_z},0\right) = 0\ \&\ C\left(\frac{r}{R_z},0\right) = 0$$

$$\text{at } \frac{r}{R_z} \in [0, 1]$$

$$u\left(\frac{r}{R_z},t\right) = 0,\ v\left(\frac{r}{R_z},t\right) = 0,\ \theta\left(\frac{r}{R_z},t\right) = 0\ \&\ C\left(\frac{r}{R_z},t\right) = 0$$

$$\text{at } \frac{r}{R_z} = 1 \quad (14)$$

After dropping * notation and considered fractional derivative, equations (10-14) can be expressed as,

$$D_t^\alpha u = b_0 + b_1\cos(\omega t) + \frac{1}{R_e}\left(1 + \frac{1}{\gamma}\right)\left[\frac{\partial^2 u}{\partial r^2} + \frac{1}{r}\frac{\partial u}{\partial r}\right] + R(v - u)$$

$$-Ha^2 u + \frac{\sin \emptyset}{F} \quad (15)$$

$$GD_t^\alpha v = u - v, \quad (16)$$

$$P_e D_t^\alpha \theta = \left(\frac{\partial^2\theta}{\partial r^2} + \frac{1}{r}\frac{\partial\theta}{\partial r}\right) + P_e(Q_m + \theta_m), \quad (17)$$

$$S_c R_e D_t^\alpha C = \left(\frac{\partial^2 C}{\partial r^2} + \frac{1}{r}\frac{\partial C}{\partial r}\right) + S_r S_c\left(\frac{\partial^2\theta}{\partial r^2} + \frac{1}{r}\frac{\partial\theta}{\partial r}\right) - S_c R_e^2 KrC \quad (18)$$

with boundary conditions

$$u\left(\frac{r}{R_z},0\right) = 0,\ v\left(\frac{r}{R_z},0\right) = 0,\ \theta\left(\frac{r}{R_z},0\right) = 0\ \&\ C\left(\frac{r}{R_z},0\right) = 0$$

$$\text{at } \frac{r}{R_z} \in [0, 1]$$

$$u\left(\frac{r}{R_z},t\right) = 0,\ v\left(\frac{r}{R_z},t\right) = 0,\ \theta\left(\frac{r}{R_z},t\right) = 0\ \&\ C\left(\frac{r}{R_z},t\right) = 0 \text{ at } \frac{r}{R_z} = 1 \quad (19)$$

Where, Caputo-Fabrizio operator is

$${}^{CF}D_t^\alpha u(r,t) = \frac{1}{1-\alpha}\int_0^t \exp\left(-\frac{\alpha(t-\tau)}{1-\alpha}\right)\frac{\partial u(r,\tau)}{\partial\tau}\,d\tau \quad (20)$$

The definition Laplace Transform for the operator of Caputo-Fabrizio expresses as,

$$L\{{}^{CF}D_t^\alpha u(r,t)\} = \frac{sL\{u(r,t) - u(r,0)\}}{(1-\alpha)s + \alpha} \quad (21)$$

With α $(0 < \alpha < 1)$ is the fractional order parameter.

Here, $\beta = \frac{1}{R_e}\left(1 + \frac{1}{\gamma}\right)$, $Ha = B_0\sqrt{\frac{\sigma \sin\theta}{\rho}}$, $F = \frac{R_0}{u_0 g}$ $\theta = \frac{T - T_\omega}{T_\omega - T_\infty}$,

$P_r = \frac{K}{\rho c_p}$, $R_e = \frac{R_z^2}{v}$, $P_e = R_e \cdot P_r$, $S_c = \frac{\nu}{\lambda D_m}$, $C = \frac{c - c_\omega}{c_\omega - c_\infty}$,

$Q_m = \frac{R_0\overline{Q_m}}{u_0\rho c_p(T_\omega - T_\infty)}$, $\theta_m = \frac{R_0\overline{\theta_m}}{u_0\rho c_p(T_\omega - T_\infty)}$

3. Solution of the problem

Now, we are using the techniques of Laplace transform in equations (15) to (19), we get

$$\frac{S\bar{u}(r,s)}{S + \alpha(1-s)} = \frac{b_0}{S} + \frac{b_1 S}{s^2 + \omega^2} + \beta_1\left(\frac{\partial^2\bar{u}(r,s)}{\partial r^2} + \frac{1}{r}\frac{\partial\bar{u}(r,s)}{\partial r}\right)$$

(22)

$$+R\bar{v} - (R + Ha^2)\bar{u}(r,s) + \frac{\sin\phi}{SF} \quad (22)$$

$$G\frac{S\bar{v}(r,s)}{S + \alpha(1-s)} = \bar{u}(r,s) - \bar{v}(r,s) \quad (23)$$

$$P_e\frac{S\bar{\theta}(r,s)}{S + \alpha(1-s)} = \left[\frac{\partial^2\bar{\theta}(r,s)}{\partial r^2} + \frac{1}{r}\frac{\partial\bar{\theta}(r,s)}{\partial r}\right] + P_e\frac{Q_m + \theta_m}{S} \quad (24)$$

$$R_eS_c\frac{S\overline{C}(r,s)}{S+\alpha(1-s)} = \left(\frac{\partial^2\overline{C}(r,s)}{\partial r^2}+\frac{1}{r}\frac{\partial\overline{C}(r,s)}{\partial r}\right) + S_rS_c\left(\frac{\partial^2\overline{\theta}(r,s)}{\partial r^2}+\frac{1}{r}\frac{\partial\overline{\theta}(r,s)}{\partial r}\right) - S_cKrR_e^2\overline{\Phi}(r,s) \tag{25}$$

With boundary condition $\bar{u}(1,s)=\bar{v}(1,s)=\bar{\theta}(1,s)=0$ from equation (23),

$$\bar{v}(r,s) = \frac{\alpha(1-\alpha)+S}{\alpha(1-s)+S+GS}\bar{u}(r,s) \tag{26}$$

Inputs equation (26) into equation (22),

$$\left[\frac{s}{S+\alpha(1-S)} - R\left(\frac{S+\alpha(1-\alpha)}{GS+S+\alpha(1-s)}\right)+R+Ha^2\right]\bar{u}(r,s) = \frac{b_0}{S}+\frac{b_1S}{s^2+\omega^2}+\beta_1\left(\frac{\partial^2\bar{u}}{\partial r^2}+\frac{1}{r}\frac{\partial\bar{u}}{\partial r}\right)+\frac{\sin\phi}{SF} \tag{27}$$

By applying Zeroth order transformation of Finite Hankel in equations (27) and (22) with boundary condition (19), we obtain the following equation.

$$\left[\frac{s}{\alpha(1-S)+S} - \left(\frac{S+\alpha(1-\alpha)}{GS+S+\alpha(1-s)}\right)R+R+Ha^2\right]\bar{u}_H(r_n,s) = \left[\frac{\sin\phi}{SF}+\frac{b_1S}{s^2+\omega^2}+\frac{b_0}{S}\right]\frac{J_1(r_n)}{r_n} - r_n\beta_1\bar{u}_H(r_n,s) \tag{28}$$

$$P_e\frac{s\overline{\theta}_H(r_n,s)}{S+\alpha(1-s)} = -r_n\overline{\theta}_H(r_n,s)+P_e\frac{Q_m+\theta_m}{S}\cdot\frac{J_1(r_n)}{r_n} \tag{29}$$

$$R_eS_c\frac{S\overline{C}_H(r,s)}{S+\alpha(1-s)} = -r_n\overline{C}_H(r_n,s)+S_rS_c(-r_n)\overline{\theta}_H(r_n,s) - S_cKr\,R_e^2\overline{C}_H(r_n,s) \tag{30}$$

Where, the Finite Hankle transformation for Temperature and velocity is given by, $\bar{u}_H(r_n,s) = \int_0^1 r\cdot\bar{u}(r,s)J_0(r_n,r)dr$

Where, J_0 is Zeroth order Bessel's function of the first kind is $J_0(x)=0$ and the positive roots are r_n

Re-Writing the equation from (28) to (30),

we get,

$$\bar{u}_H(r_n,s) = \frac{S^2B_5+SB_6+\alpha^2}{S^2B_2+SB_3+B_4}\left[\frac{1}{S}\left(b_0+\frac{\sin\phi}{F}+\frac{b_1S}{s^2+\omega^2}\right]\frac{J_1(r_n)}{r_n} \tag{31}$$

$$\therefore\ \bar{u}_H(r_n,s) = \left[\frac{B_9}{S-B_7}+\frac{B_{10}}{S-B_8}\right]\left[\frac{1}{S}\left(b_0+\frac{\sin\phi}{F}+\frac{b_1S}{s^2+\omega^2}\right]\frac{J_1(r_n)}{r_n} \tag{32}$$

$$\therefore\ \bar{u}_H(r_n,s) = \left(b_0+\frac{\sin\phi}{F}\right)\left[B_9\frac{S^{-1}}{S-B_7}+B_{10}\frac{S^{-1}}{S-B_8}\right]\frac{J_1(r_n)}{r_n} + \frac{b_1S}{s^2+\omega^2}\left[\frac{1}{S-B_7}B_9+\frac{1}{S-B_8}B_{10}\right]\frac{J_1(r_n)}{r_n} \tag{33}$$

In same manner we proceed for Energy equation (29), we get

$$\overline{\theta}_H(r_n,s) = \frac{P_e(Q_m+\theta_m)}{S\left[r_n+P_e\frac{S}{S+\alpha(1-s)}\right]}\cdot\frac{J_1(r_n)}{r_n} \tag{34}$$

Now, rearrange the equation (33)

$$\overline{\theta}_H(r_n,s) = \left[\frac{1}{S+B_{15}}B_{13}+\frac{1}{S-B_{15}}B_{14}\right]\frac{J_1(r_n)}{r_n} \tag{35}$$

In same manner we proceed for Concentration equation (30), we get

$$\frac{R_eS_c\cdot S\overline{C}_H(r,s)}{S+\alpha(1-s)} = \left[\frac{S_rS_c(-r_n)P_e(Q_m+\theta_m)}{S\left[r_n+P_e\frac{S}{S+\alpha(1-s)}\right]}\right]\cdot\frac{J_1(r_n)}{r_n} - S_cKrR_e^2\overline{C}_H(r_n,s) - r_n\overline{C}_H(r_n,s) \tag{36}$$

$$\left[\frac{R_eS_c\cdot S}{S+\alpha(1-s)}+S_cKrR_e^2+r_n\right]\overline{C}_H(r,s) = \left[\frac{-r_nS_rS_cP_e(Q_m+\theta_m)}{S\left[r_n+P_e\frac{S}{S+\alpha(1-s)}\right]}\right]\cdot\frac{J_1(r_n)}{r_n} \tag{37}$$

$$\overline{C}_H(r,s) = -\frac{S_rS_cr_nP_e(Q_m+\theta_m)}{\left(S\left[r_n+P_e\frac{S}{S+\alpha(1-s)}\right]\right)\left[\frac{R_eS_c\cdot S}{S+\alpha(1-s)}+r_n+S_cK_cR_e^2\right]}\cdot\frac{J_1(r_n)}{r_n} \tag{38}$$

Now, rearrange the equation (37)

$$\overline{C}_H(r,s) = \frac{B_{16}}{\left(S\left[B_{17}+P_e\frac{S}{S+\alpha(1-s)}\right]\right)\left[\frac{B_{19}\cdot S}{S+\alpha(1-s)}+r_n+B_{18}\right]}\cdot\frac{J_1(r_n)}{r_n} \tag{39}$$

$$\overline{C}_H(r,s) = \frac{B_{16}(S+\alpha(1-S))^2}{S(B_{17}S+B_{17}\alpha-B_{17}\alpha S+P_eS)(B_{19}S+B_{18}\alpha+B_{18}S-B_{18}\alpha S)}\cdot\frac{J_1(r_n)}{r_n} \tag{40}$$

$$\overline{C}_H(r,s) = \frac{B_{16}(S+\alpha(1-S))^2}{S((B_{17}-B_{17}\alpha+P_e)S+B_{17}\alpha)((B_{19}+B_{18}-B_{18}\alpha)S+B_{18}\alpha)}\cdot\frac{J_1(r_n)}{r_n} \tag{41}$$

$$\overline{C}_H(r,s) = \frac{B_{16}(S+\alpha(1-S))^2}{S(B_{20}S+B_{22})(B_{21}S+B_{23})}\cdot\frac{J_1(r_n)}{r_n} \tag{42}$$

$$\overline{C}_H(r,s) = \frac{B_{16}}{B_{20}\cdot B_{21}}\frac{(\alpha^2+2\alpha(1-\alpha)S+(1-\alpha)^2S^2)}{S\left(S+\frac{B_{22}}{B_{20}}\right)\left(S+\frac{B_{23}}{B_{21}}\right)}\cdot\frac{J_1(r_n)}{r_n} \tag{43}$$

$$\overline{C}_H(r,s) = \frac{B_{16}}{B_{20}\cdot B_{21}}\frac{(\alpha^2+2\alpha(1-\alpha)S+(1-\alpha)^2S^2)}{S\left(S+\frac{B_{22}}{B_{20}}\right)\left(S+\frac{B_{23}}{B_{21}}\right)}\cdot\frac{J_1(r_n)}{r_n} \tag{44}$$

$$\overline{C}_H(r,s) = \frac{B_{24}(\alpha^2+B_{25}S+B_{26}S^2)}{S(S+B_{27})(S+B_{28})}\cdot\frac{J_1(r_n)}{r_n} \tag{45}$$

$$\overline{C}_H(r,s) = \left(\frac{B_{29}}{S}+\frac{B_{30}}{S+B_{27}}+\frac{B_{29}}{S+B_{28}}\right)\cdot\frac{J_1(r_n)}{r_n} \tag{46}$$

Using the concept of Robotnov and Hartley's function the Inverse Laplace transform is,

$$LT^{-1}\left[\frac{1}{S^{\omega+y}}\right] = F_\omega(-y,t) = \sum_{n=0}^{\infty}\frac{(-y)^n t^{(n+1)w-1}}{\Gamma((n+1)w)};\ \omega>0 \tag{47}$$

$$LT^{-1}\left[\frac{S^z}{S^{w+y}}\right] = R_{w,z}(-y,t) = \sum_{n=0}^{\infty}\frac{(-y)^n t^{(n+1)w-1-z}}{\Gamma((n+1)w-z)};\ Re(w-z)>0 \tag{48}$$

Now, we apply Inverse Laplace transform of equations (33), (35) and (46) are

$$\therefore\ \overline{u}_H(r_n,t) = \frac{J_1(r_n)}{r_n}\Big[(e^{B_7 t}-1)\Big(\frac{b_0}{B_7}B_9 + \frac{B_9\sin\phi}{B_7 F}\Big) + (e^{B_8 t}-1)\Big(\frac{b_0}{B_8}B_{10} + \frac{B_{10}\sin\phi}{B_8 F}\Big) + b_1 B_9 e^{B_7 t} * \cos(\omega t) + b_1 B_{10} e^{B_8 t} * \cos(\omega t)\Big] \tag{50}$$

$$= \frac{J_1(r_n)}{r_n}[B_{13}F_1(-B_{15},t) + B_{14}R_{i-1}(-B_{15},t)] \tag{51}$$

By applying Inverse Hankle transformation technique we obtain fluid velocity and Temperature equations (49), (51), and (52),

$$\therefore\ \overline{C}_H(r_n,t) = \frac{J_1(r_n)}{r_n}[B_{29} + B_{30}e^{-B_{27}t} + B_{31}e^{-B_{31}t}] \tag{52}$$

$$u(r,t) = 2\sum_{n=1}^{\infty}\frac{J_0(\frac{r}{r_z}r_n)}{r_n J_1^2(r_n)} \times u_H(r_n,t) \tag{53}$$

$$u(r,t) = 2\sum_{n=1}^{\infty}\frac{J_0(\frac{r}{r_z}r_n)}{r_n J_1^2(r_n)}[(e^{B_7 t}-1)(\frac{b_0}{B_7}B_9 + \frac{B_9\sin\phi}{B_7 F}) + (e^{B_8 t}-1)(\frac{b_0}{B_8}B_{10} + \frac{B_{10}\sin\phi}{B_8 F}) + b_1 B_9 e^{B_7 t} + \cos(\omega t) + b_1 B_{10} e^{B_8 t} + \cos(\omega t)] \tag{54}$$

$$\theta(r,t) = 2\sum_{n=1}^{\infty}\frac{J_0(\frac{r}{r_z}r_n)}{r_n J_1^2(r_n)} \times \theta_H(r_n,t) \tag{55}$$

$$\theta(r,t) = 2\sum_{n=1}^{\infty}\frac{J_0(\frac{r}{r_z}r_n)}{r_n J_1^2(r_n)} \times [B_{13}e^{-B_{15}t} + \frac{B_{14}}{B_{15}}(1-e^{-B_{15}t})] \tag{56}$$

$$C(r,t) = 2\sum_{n=1}^{\infty}\frac{J_0(\frac{r}{r_z}r_n)}{r_n J_1^2(r_n)} \times C_H(r_n,t) \tag{57}$$

$$C(r,t) = 2\sum_{n=1}^{\infty}\frac{J_0(\frac{r}{r_z}r_n)}{r_n J_1^2(r_n)} \times [B_{29} + B_{30}e^{-B_{27}t} + B_{31}e^{-B_{31}t}] \tag{58}$$

Velocity of magnetic particles is represented from equation (24)

$$\overline{v}(r,s) = \frac{S+\alpha-\alpha s}{GS+S+\alpha(1-s)}\overline{u}(r,s) \tag{59}$$

$$v(r,t) = B_{33}(1-B_{32})[u(r,t)^{*}\ e^{B_{12}t}],\ 0<\alpha<1 \tag{60}$$

4. Result and discussion

In this paper, we have investigated the influences of different parameters on the artery in the presence of multiple stenoses. Figure 2 presents the variation of blood flow velocity across the radial axis for varying systolic pressure gradients (a_0=0.5,1,1.5). An increase in pressure gradient leads to a corresponding increase in peak blood velocity. This occurs because systolic pressure, the highest pressure during that time, exerts a strong force on the blood, increasing its velocity. 78% rise is noted with increasing systolic pressure gradient from 0.5 to 1, This result agreed with the previous published work done by Patel et al. [34]. In this graph, the maximum velocity occurs at the center of the artery and decreases symmetrically towards the walls, where it becomes zero due to the no-slip boundary conditions. This will identify laminar characteristics of flow and show that systolic pressures enhance the flow rate, which could significantly influence blood dynamics in a diseased arterial segment.

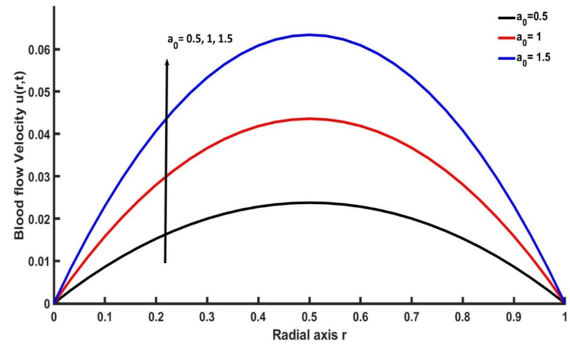

Figure 2. a_0 on u

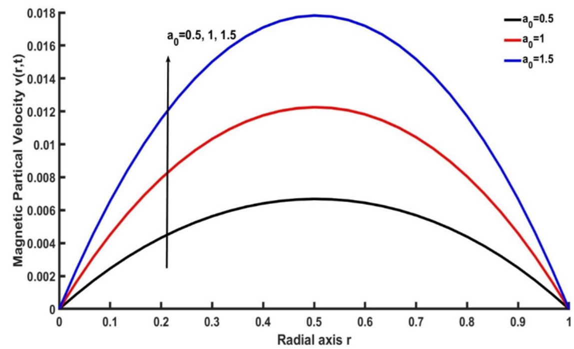

Figure 3. a_0 on v

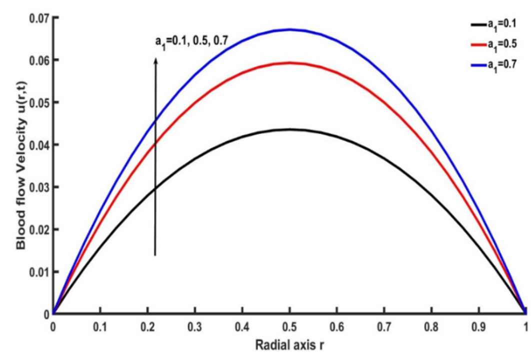

Figure 4. a_1 on u

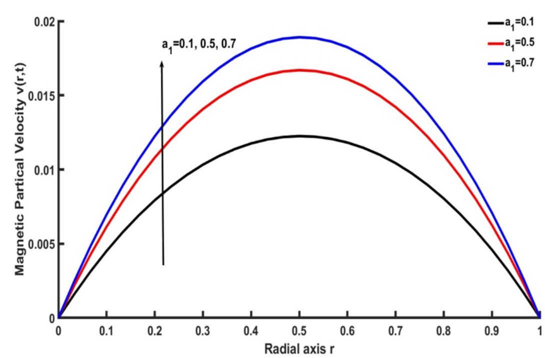

Figure 5. a_1 on v

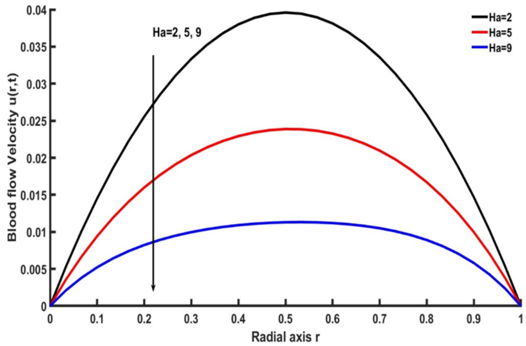

Figure 6. H_a on u

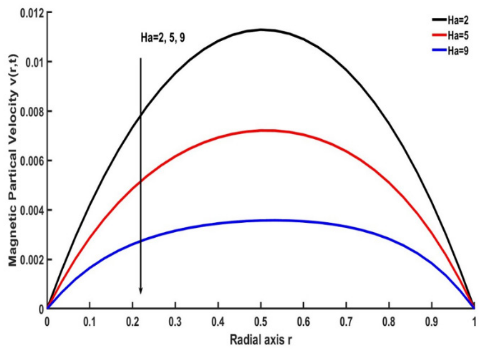

Figure 7. H_a on v

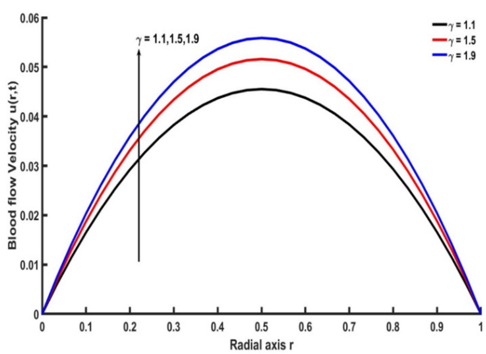

Figure 8. γ on u

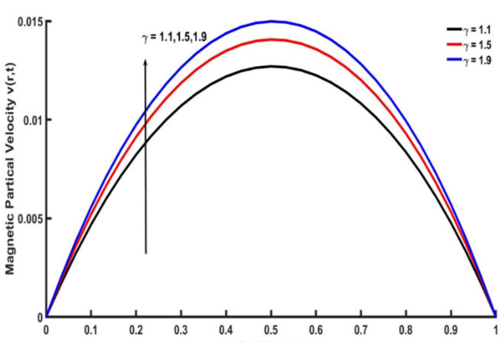

Figure 9. γ on v

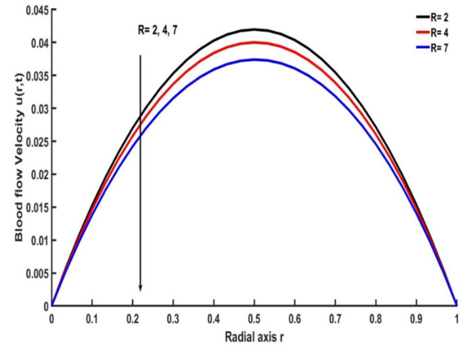

Figure 10. R on u

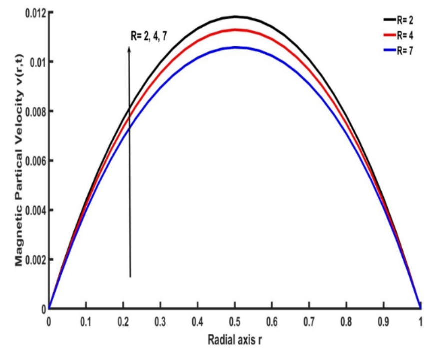

Figure 11. R on v

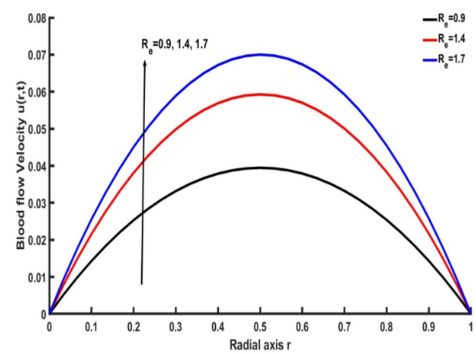

Figure 12. R_e on u

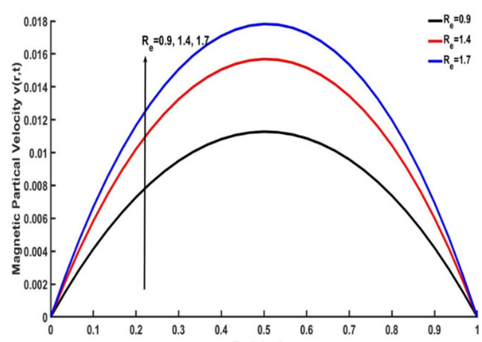

Figure 13. R_e on v

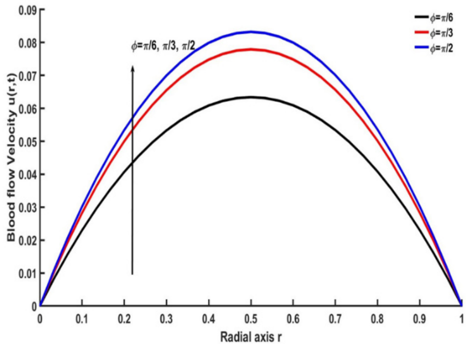

Figure 14. ϕ on u

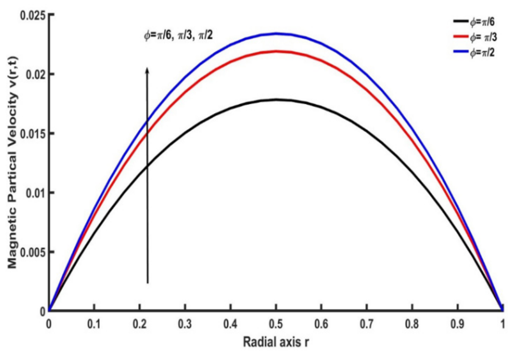

Figure 15. ϕ on v

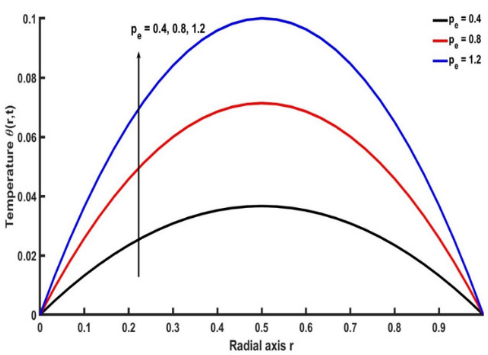

Figure 16. p_e on θ

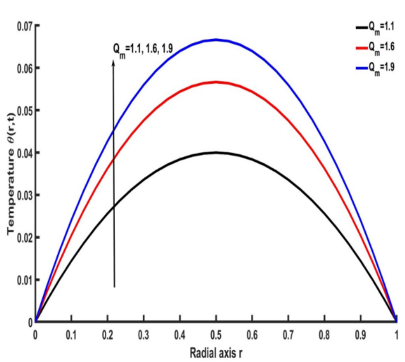

Figure 17. Q_m on θ

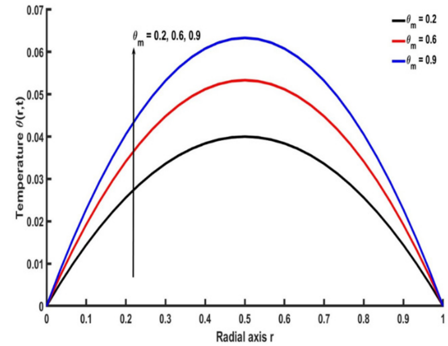

Figure 18. θ_m on θ

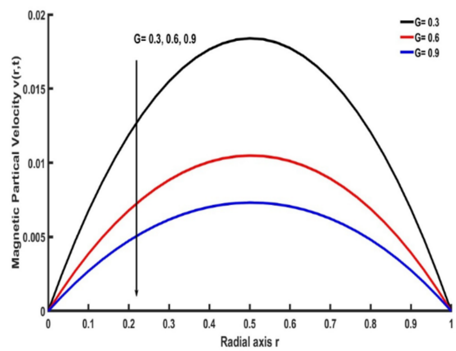

Figure 19. G on v

Figure 3 shows the radial variation of the velocity of a magnetic particle for distinct pressure gradients. Magnetic particle velocity also increases with the systolic pressure gradient, particularly near the center of the artery, because the increased blood velocity associated with systolic pressure enhances their motion. This behavior reflects an increased axial driving force imparted by elevated pressure, which enhances particle transport through stenosed arterial segments. The results highlight the direct impacts of pressure conditions on targeted drug delivery using magnetic transporters. In Figure 4, the impact of the diastolic pressure gradient on a Casson fluid is presented. An overall increase in velocity magnitude is observed due to higher diastolic pressure gradients, particularly near the central axis of the artery. These changes occur because an increase in diastolic pressure creates a large pressure differential that drives flow, especially at the narrowed portion of the artery. A 67% rise in blood flow velocity was as the diastolic pressure gradient increased from 0.1 to 0.5. This indicates that even during diastole, an elevated pressure gradient sustains a stronger flow through the stenosed regions. Figure 5 displays the change in magnetic particle velocity under an increasing diastolic pressure gradient. The diastolic pressure gradient increases along with an upward trend in particle velocity, with the peak velocity occurring near the arterial centerline, because increasing blood flow velocity also enhances the velocity of magnetic particles. Diastolic pressure effectively maintains magnetic particle motion, which supports therapeutic delivery during both phases of the cardiac cycle. Figure 6 shows a noticeable reduction in blood flow velocity as the Hartmann number increases, indicating that stronger magnetic fields significantly dampen flow. Increasing Hartmann number from 2 to 9 will decrease blood flow velocity by up to 40%. The reason is that increasing the Hartmann induces a strong Lorentz force opposing the direction of blood flow, thereby increasing resistance to blood flow. In practice, this is common in medical applications such as magnetic drug targeting or MRI-guided therapies, where magnetic fields are used to influence blood flow or particle movement. It can be seen that the flow remains laminar but is controlled, as the parabolic shape of the velocity profile persists. Figure 7 illustrates how the magnetic particle velocity changes along the radial axis for three increasing values of the Hartmann number. A noticeable decline in particle velocity is observed with increasing Hartmann number, particularly near the central region of the artery. Decreasing blood velocity will slow magnetic particle motion. This trend signifies the damping effect of the magnetic field, which resists particle motion and reduces axial transport. Such behavior underscores the role of magnetic field strength in regulating particle dynamics during magnetically guided drug delivery. Figure 8 shows the effects of the Casson fluid parameter on magnetic particle velocity. As the Casson fluid parameter increases, the velocity profile becomes steeper, with higher velocities concentrated near the center of the artery. This reflects a reduction in the fluid's yield stress, allowing particles to move more smoothly under the same driving pressure. The findings emphasize that non-Newtonian properties of blood, influenced by the Casson fluid parameter, can enhance the efficiency of magnetic particle transport in therapeutic applications. Figure 9 supports the understanding that magnetic particle velocity increases with rising non-dimensional Casson fluid parameter. From the figure, it is obvious that the particle velocity rises noticeably near the center of the artery as the Casson fluid parameter increases. This will help particles move more smoothly due to the reduction in fluid yield stress at the same pressure. This study contributes to understanding the role of fluid rheology in enhancing the transport of magnetic carriers, a process critical for efficient, targeted drug delivery in Casson-type blood flows. Figure 10 demonstrates that, with increasing non-dimensional concentration, blood flow velocity decreases; a regular reduction in velocity is observed in the central portion of the artery. The main of this phenomenon is that high concentration increases viscosity and enhances particle-fluid interaction. This is useful for concluding that high solute concentration increases fluid resistance, which could be a primary cause of reduced blood flow velocity. This scenario is the same as a pathological condition, such as plaque accumulation. Figure 11 shows the changes in magnetic-particle velocity along the radial axis due to an increasing value of the nondimensional concentration parameter of the magnetic particles. It can be concluded that the magnetic-particle concentration gradually decreases with increasing values of the non-dimensional concentration parameter. Due to the increasing interaction among fluid particles, magnetic particles will also face resistance. This effect is clearly visible in the central portion of the artery. Extreme solute concentrations may increase drag forces or micro-interactions, limiting particle mobility. In the magnetic particle therapies, this behavior is crucial, because precise control over particle transport is required. Figure 12 reveals that, particularly in the core region, a rising Reynolds number will significantly increase blood flow velocity. Increasing the Reynolds number causes inertial forces to dominate, allowing the fluid to flow more freely. This result is strongly agreed with previous work done by Patel et al. [34], and comparison reveal high similarity in blood flow velocity along with increasing Reynold number. This promotes more vigorous flow by enhancing inertial forces that overcome viscous resistance. The results emphasize the critical role of the flow regime in the dynamics of stenosed arteries. Figure 13 shows the influence of the Reynolds number on the increase in magnetic particle velocity. Up to a 40% rise in magnetic particles was noted as the Reynolds number increased from 0.9 to 1.4. Thus, a higher Reynolds number is sufficient to enhance particle mobility. These findings suggest a favorable condition for magnetically guided drug delivery under elevated flow rates. Figure 14 illustrates that increasing the inclination angle causes a noticeable rise in velocity near the central region of the artery. This is because a higher reduces the opposing gravitational force, thereby permitting faster flow. This trend is attributed to the altered orientation of the stenosed geometry, which reduces flow resistance and enables more efficient axial transport. The results suggest that increased inclination enhances blood perfusion in narrowed arterial segments. Figure 15 shows, along the radial axis, the effects on the velocity of magnetic particles especially at the core of the artery as the inclination angle increases from $\pi/6$ to $\pi/2$, because the increased blood flow velocity associated with a larger inclination angle influences the movement of magnetic particles in the radial direction. This improves streamline formation because steeper arterial alignments facilitate axial particle propulsion. This study is useful for designing targeted drug delivery systems based on the geometrical orientation of multi-stenosed arteries. Figure 16 illustrates the influence of the Peclet number on the temperature profile. As the Peclet number increases, the temperature within the artery rises significantly. This is because increasing the Peclet number will increase convection within the blood flow, which will be the main cause of the rise in temperature in the artery. This behavior indicates that stronger convective heat transport enhances the thermal energy carried by the fluid. Consequently, the centerline temperature becomes more pronounced, while the temperature gradient near the arterial walls steepens, reflecting increased advective dominance over conductive effects. Figure 17 displays how temperature varies in response to different levels of metabolic heat source; there is a consistent rise in temperature throughout the radial domain because increasing the metabolic heat source leads to greater internal heat generation within the artery, resulting in higher temperatures. Increasing the metabolic heat source from 1.1 to 1.6 will enhance blood flow by up to 45%. Equivalent rise in temperature profile was noted in previously published word Patel and Patel [35] with increasing metabolic heat source. Elevated temperatures indicate that internal heat generation from metabolic activity significantly contributes to the blood's thermal energy content. The peak temperature remains at the center of the artery, where the influence of the heat source is greatest, indicating stronger internal thermal accumulation as the metabolic heat source increases. Figure 18 shows that temperature increases significantly as the metabolic heat source increases. Increasing value of θ_m represent heat absorption rate will be high accordingly which implies heat is being retained within flow instead of losing will be the primary cause of increasing temperature in the artery, especially in the centreline. Figure 19 illustrates the effect of the particle-mass parameter on the magnetic-particle velocity distribution. Across the radial profile, the velocity of the magnetic particles decreases as the particle mass parameter increases. The highest velocity is achieved when the particle mass parameter is 0.3; it gradually diminishes as the particle mass increases.

5. Conclusion

This study reveals the impacts of different parameters in the presence of a multi-stenosed artery, including chemical reaction effects.

- According to the study, increased driving forces such as systolic and diastolic pressure gradients play a vital role in increasing flow and particle velocity, particularly in the central region of the artery. The increasing systolic pressure gradient accelerates blood flow towards the center, as in the real-life scenario of a blocked artery. These modifications may restore normal blood flow in the stenosed artery.
- Magnetic fields, as represented by the Hartmann number, slow blood flow, which is beneficial for controlled, targeted drug delivery. Magnetic fields applied at different angles effectively reduce strokes, swelling, and pain. An increased Hartmann number reduces blood velocity. Research into the treatment of atherosclerosis will benefit from this information.
- Metabolic heat absorption and generation will substantially affect temperature. Increasing temperature, together with changes in internal flow and heat, can play a significant role in regulating treatment behavior. Due to heat generation, blood viscosity decreases, blood becomes thinner, and flow accelerates.
- Geometry and flow strength improve delivery paths, excessive resistance or heavier particles can slow transport.
- Together, these findings offer valuable insights to inform the design of more efficient, controlled drug-delivery systems for diseased arteries.

Authorship contributions

Authors equally contributed to this work.

Data availability statement

The authors confirm that the data that supports the findings of this study are available within the article. Raw data that support the finding of this study are available from the corresponding author, upon reasonable request.

Conflict of interest

The author declared no potential conflicts of interest with respect to the research, authorship, and/or publication of this article.

Ethics

There are no ethical issues with the publication of this manuscript.

Statement on the use of artificial intelligence

Artificial intelligence was not used in the preparation of the article.

Nomenclature

Symbol	
a_0	Systolic Pressure gradient
a_1	Diastolic Pressure gradient
$\vec{B}$	Magnetic Field
γ	Casson fluid parameter
ω	Pulsatile frequency
R	Non – dimensional particle concentration parameter
H_a	Non – dimensional Hartman number
ϕ	Phase angle
F	Inclination angle parameter
P	Oscillating pressure gradient
R_e	Reynolds number
P_e	Peclet Number
Q_m	Metabolic Heat Source
θ_m	Metabolic Heat absorption
G	Particle mass parameter
ρ	Fluid density
r	Radial coordinator
α	Fractional parameter
σ	Electrical conductivity
u(r,t)	The velocity of the Fluid
ν(r,t)	The velocity of the Particle
N	Magnetic particles number
K	Stokes constant
υ	Kinematic viscosity
S_c	Schmidt number
Kr	Chemical reaction Parameter
β_0	Magnetic Field strength

g	Gravitational acceleration
m	Mass of acceleration
K_1	Thermal Conductivity of blood
C_p	Specific heat Capacity of blood
C	Concentration of diffusion species
D_m	Mass Diffusivity
K_T	Thermal diffusion ration
T_∞	Ambient Temperature
C_∞	Reference Concentration

References

[1] Dash, R. K., Mehta, K. N., & Jayaraman, G. (1996). Casson fluid flow in a pipe filled with a homogeneous porous medium. International Journal of Engineering Science, 34(10), 1145-1156.

[2] Ali, A., Hussain, S., & Ashraf, M. (2024). Theoretical investigation of unsteady MHD flow of Casson hybrid nanofluid in porous medium: Applications of thermal radiations and nanoparticle. Journal of Radiation Research and Applied Sciences, 17(3),101029.

[3] Raghunatha, K. R., Vinod, Y., Nagappanavar, S. N., & Sangamesh. (2023). Unsteady Casson fluid flow on MHD with an internal heat source. Journal of Taibah University for Science, 17(1),2271691.

[4] Mukhopadhyay, S., Mondal, I. C., & Chamkha, A. J. (2013). Casson fluid flow and heat transfer past a symmetric wedge. Heat Transfer—Asian Research, 42(8),665-675.

[5] Afikuzzaman, M., & Alam, M. M. (2016). MHD casson fluid flow through a parallel plate. Science & Technology Asia, 59-70.

[6] Kataria, H., & Patel, H. (2018). Heat and mass transfer in magnetohydrodynamic (MHD)Casson fluid flow past over an oscillating vertical plate embedded in porous medium with ramped wall temperature. Propulsion and Power Research, 7(3),257-267.

[7] Nandhini, C. A., Jothimani, S., & Chamkha, A. J. (2025). Synergy of non-uniform heat source/sink and variable thermal conductivity on stagnation point flow of Casson fluid over a convective stretching sheet. Journal of Thermal Engineering, 11(1),254-269.

[8] Gupta, S., Sharma, P. K., Kumar, S., & Tiwari, C. M. (2024). Influence of buoyancy forces in MHD non-Newtonian convective nanofluid utilizing Buongiorno's Model induced by 3D exponential sheet. Journal of Thermal Engineering, 10(5),1107-1119.

[9] Dang, K., Makkar, V., & Sharma, N. (2024). Numerical analysis of three-dimensional magnetohydrodynamics non-Newtonian free stream flow induced by permeable stretching surface. Journal of Thermal Engineering, 10(6),1465-1479.

[10] Makkar, V., & Poply, V. (2021). Impact of outer velocity on flow, heat and mass transfer of Casson nanofluid over a non-linear stretching sheet. Journal of Thermal Engineering, 7(6),1353-1365.

[11] Nandeppanavar, M. M. (2018). Melting heat transfer analysis of non-Newtonian Casson fluid due to moving plate. Engineering Computations, 35(3), 1301-1313.

[12] Zaib, A., Bhattacharyya, K., Uddin, M. S., & Shafie, S. (2016). Dual solutions of non-Newtonian Casson fluid flow and heat transfer over an exponentially permeable shrinking sheet with viscous dissipation. Modelling and simulation in engineering, 2016(1),6968371.

[13] Hayat, S. Asad, and A. Alsaedi, "Flow of Casson fluid with nanoparticles," Applied Mathematics and Mechanics, vol. 37, no. 4, pp. 459–470, 2016.

[14] Roy, M., Sikarwar, B. S., Bhandwal, M., & Ranjan, P. (2017). Modelling of blood flow in stenosed arteries. Procedia Computer Science, 115, 821-830.

[15] Ismail, Z., Abdullah, I., Mustapha, N., & Amin, N. (2008). A power-law model of blood flow through a tapered overlapping stenosed artery. Applied Mathematics and Computation, 195(2),669-680.

[16] Bakheet, A., Alnussaiyri, E. A., Ismail, Z., & Amin, N. (2016). Blood flow through an inclined stenosed artery. Applied Mathematical Sciences, 10(5-8),235-254.

[17] Ku, D. N. (1997). Blood flow in arteries. Annual review of fluid mechanics, 29(1),399-434.

[18] Akhtar, S., Hussain, Z., Nadeem, S., Najjar, I. R., & Sadoun, A. M. (2023). CFD analysis on blood flow inside a symmetric stenosed artery: Physiology of a coronary artery disease. Science progress, 106(2),00368504231180092.

[19] Charkravarty, S., & Sen, S. (2005). Dynamic response of heat and mass transfer in blood flow through stenosed bifurcated arteries. Korea-Australia Rheology Journal, 17(2),47-62.

[20] Mwapinga, A. (2024). Mathematical formulation and computation of the dynamics of blood flow, heat and mass transfer during MRI scanning. Scientific Reports, 14(1),6364.

[21] Deka, B., & Choudhury, R. (2025). MHD stream past an inclined surface with diffusion-thermo and viscous dissipation sequels. Journal of Thermal Engineering, 11(3),800-810.

[22] Jamil, D. F. (2022). Caputo-fabrizio fractional derivative for magnetic blood flow of Newtonian and casson fluid in an inclined artery (Doctoral dissertation, Universiti Tun Hussein Onn Malaysia).

[23] Rahman, M. U., Althobaiti, A., Riaz, M. B., & Al-Duais, F. S. (2022). A theoretical and numerical study on fractional order biological models with Caputo Fabrizio derivative. Fractal and Fractional, 6(8),446.

[24] Ahmed, I., Akgül, A., Jarad, F., Kumam, P., & Nonlaopon, K. (2023). A Caputo-Fabrizio fractional-order cholera model and its sensitivity analysis. Mathematical Modelling and Numerical Simulation with Applications, 3(2),170-187.

[25] Jain, N., & Divecha, N. H. (2023, December). An Improved Grunwald-Letnikov Fractional Order Differential Operator for Image Enhancement. In International Conference on Computational Modeling and Sustainable Energy (pp. 267-278). Singapore: Springer Nature Singapore.

[26] Kataria, H. R., & Patel, H. R. (2016). Radiation and chemical reaction effects on MHD Casson fluid flow past an oscillating vertical plate embedded in porous medium. Alexandria Engineering Journal, 55(1),583-595.

[27] Patel, H. R. (2022). Soret and heat generation effects on unsteady MHD Casson fluid flow in porous medium. Waves in Random and Complex Media, 35(1),1172–1195.

[28] Shahzad, M. H., Nadeem, S., Awan, A. U., Allahyani, S. A., Ahammad, N. A., & Eldin, S. M.(2024).On the steady flow of non-Newtonian fluid through multi-stenosed elliptical artery: a theoretical model. Ain Shams Engineering Journal, 15(1),102262.

[29] Kabir, M. A., Alam, M. F., & Uddin, M. A. (2021). Numerical simulation of pulsatile blood flow: a study with normal artery, and arteries with single and multiple stenosis. Journal of Engineering and Applied Science, 68, 1-15.

[30] Yadav, S., Kumar, S., Sharma, P. K., Makkar, V., & Dang, K. (2025). Numerical modelling of 3D magnetohydrodynamics chemically reacting permeable sheet influenced by free stream convection nanofluid flow. Journal of Thermal Engineering, 11(3),845-857.

[31] F. Jamil et al., "Analysis of non-Newtonian magnetic Casson blood flow in an inclined stenosed artery using Caputo-Fabrizio fractional derivatives," Computer Methods and Programs in Biomedicine., 203 (2021) 106044. doi: 10.1016/j.cmpb.2021.106044.

[32] Hayat T, Shehzad S A, Alsaedi A, Soret and Dufour effects on magnetohydrodynamic (MHD) flow of Casson fluid, Applied Mathematics and Mechanics, 33(2012)1301-1312.

[33] Ali Shah, D. Vieru, and C. Fetecau, "Effects of the fractional order and magnetic field on the blood flow in cylindrical domains," Journal of Magnetism and Magnetic Materials, 409 (2016) 10–19. doi: 10.1016/j.jmmm.2016.02.013.

[34] Patel, Harshad and Patel, Nilesh and Patel, Snehal, Fractional Order Simulation of Casson Blood Flow in an Inclined Muti-Stenosed Artery with Magnetic Fields Effects. Available at SRN: https://ssrn.com/abstract=4674756

[35] Patel, N., & Patel, H. (2025). Thermo-Diffusion Effects on Fractional Ordered Model of Unsteady Casson Blood Flow with Magnetic Field Effect. Contemporary Mathematics, 288-306. 10.37256/cm.6120252609

Appendix

$$B_1 = R + Ha^2 + B_1 r_n^2$$

$$B_2 = 1 + G - \alpha - R - R\alpha^2 + 2R\alpha + B_1 + B_1\alpha^2 - 2\alpha B_1 + GB_1 - G\alpha B_1$$

$$B_3 = \alpha + 2R\alpha^2 - 2R\alpha - 2B_1\alpha^2 + 2\alpha B_1 + G\alpha B_1$$

$$B_4 = B_1\alpha^2 - R\alpha^2, B_5 = 1 + \alpha^2 - 2\alpha + G + G\alpha, B_6 = -2\alpha^2 + 2\alpha + G\alpha$$

$$B_7 = \frac{-B_3 \pm \sqrt{B_3^2 - 4B_2B_4}}{2B_2}, B_8 = \frac{-B_3 \pm \sqrt{B_3^2 - 4B_2B_4}}{2B_2},$$

$$B_9 = \frac{B_7^2 B_5 + B_7 B_6 + \alpha^2}{B_7 - B_8},$$

$$B_{10} = \frac{B_8^2 B_5 + B_8 B_6 + \alpha^2}{B_8 - B_7}, B_{11} = (r_n)(1 - \alpha) + P_e, B_{12} = (r_n) \cdot \alpha$$

$$B_{13} = P_e \frac{(Q_m + \theta_m)(1 - \alpha)}{B_{11}}, B_{14} = P_e \frac{(Q_m + \theta_m) \cdot \alpha}{B_{11}}, B_{15} = \frac{B_{12}}{B_{11}},$$

$$B_{16} = -S_r S_c r_n P_e (Q_m + \theta_m), B_{17} = r_n, B_{18} = r_n + S_c Kr R_e^2,$$

$$B_{19} = R_e S_c, B_{20} = B_{17} - B_{17}\alpha + P_e, B_{21} = B_{19} + B_{18} - B_{18}\alpha, B_{22} = B_{17}\alpha$$

$$B_{23} = B_{18}\alpha, B_{24} = \frac{B_{16}}{B_{20} \cdot B_{21}}, B_{25} = 2\alpha(1 - \alpha), B_{26} = (1 - \alpha)^2, B_{27} = \frac{B_{22}}{B_{20}}$$

$$B_{28} = \frac{B_{23}}{B_{21}}, B_{29} = \frac{B_{24}(\alpha^2)}{B_{27}B_{28}}, B_{30} = \frac{B_{24}(\alpha^2 + B_{25}(-B_{27}) + B_{26}(B_{27})^2)}{(-B_{27})(B_{28} - B_{27})},$$

$$B_{31} = \frac{B_{24}(\alpha^2 + B_{25}(-B_{28}) + B_{26}(B_{28})^2)}{(-B_{28})(B_{27} - B_{28})}, B_{32} = \frac{1 - \alpha}{G - \alpha + 1}, B_{33} = \frac{\alpha}{G - \alpha + 1}$$

$$f * g \text{ - convolution of } f \ \& \ g, f * g = \int_0^t f(z) g(t - z) dz$$